Crystal Structure and Transport Properties of the Homologous Compounds (PbSe)5(Bi2Se3)3m (m = 2, 3)

Selma Sassi, Christophe Candolfi, Gaëlle Delaizir, Sylvie Migot, Jaafar Ghanbaja, Christine Gendarme, Anne Dauscher, Bernard Malaman, Bertrand Lenoir

▶ To cite this version:

Selma Sassi, Christophe Candolfi, Gaëlle Delaizir, Sylvie Migot, Jaafar Ghanbaja, et al.. Crystal Structure and Transport Properties of the Homologous Compounds (PbSe)5(Bi2Se3)3m (m = 2, 3). Inorganic Chemistry, 2018, 57 (1), pp.422-434. 10.1021/acs.inorgchem.7b02656 . hal-02180362

HAL Id: hal-02180362
https://unilim.hal.science/hal-02180362

Submitted on 24 Mar 2020

Crystal Structure and Transport Properties of the Homologous Compounds $(PbSe)_5(Bi_2Se_3)_{3m}$ (m = 2 and 3)

Selma Sassi[1], Christophe Candolfi[1], Gaëlle Delaizir[2], Sylvie Migot[1], Jaafar Ghanbaja[1],
Christine Gendarme[1], Anne Dauscher[1], Bernard Malaman[1], and Bertrand Lenoir[1,*]

[1] *Institut Jean Lamour, UMR 7198 CNRS – Université de Lorraine, 2 allée André Guinier – Campus ARTEM, 54011 Nancy, France*

[2] *Sciences des Procédés Céramique et de Traitement de Surface (SPCTS), UMR CNRS 7315-Univsersité de Limoges, Limoges, France*

Abstract

We report on a detailed investigation of the crystal structure and transport properties in a broad temperature range (2 – 723 K) of the homologous compounds $(PbSe)_5(Bi_2Se_3)_{3m}$ for m = 2 and 3. Single-crystal X-ray diffraction data indicate that the m = 2 and m = 3 compounds crystallize in the monoclinic space groups $C2/m$ (No. 12) and $P2_1/m$ (No. 11), respectively. In agreement with diffraction data, high-resolution transmission electron microscopy analyses carried out on single crystals show that the three-dimensional crystal structures are built from alternate Pb-Se and m Bi-Se layers stacked along the a axis in both compounds. Scanning electron microcopy and electron-probe microanalyses reveal deviations from the nominal stoichiometry suggesting a domain of existence in the pseudo-binary phase diagram at 873 K. The complex atomic-scale structures of these compounds leads to very low lattice thermal conductivities κ_L that approach the glassy limit at high temperatures. The comparison of the κ_L values across this series unveiled an unexpected increase with increasing m from m = 1 to m = 3, contrary to the expectation that increasing the structural complexity should tend to lower the thermal transport. This result points to a decisive role played by the Pb-Se/Bi-Se interfaces in limiting κ_L in this series. Both compounds behave as heavily-doped n-type semiconductors with relatively low electrical resistivity and thermopower values. As a result, moderate peak ZT values of 0.25 and 0.20 at 700 K were achieved in the m = 2 and m = 3 compounds, respectively. The inherent poor ability of these structures to conduct heat suggests that these homologous compounds may show interesting thermoelectric properties when properly optimized by extrinsic dopants.

Introduction

Thermoelectric materials that enable solid-state conversion of heat into electricity and vice-versa can be used in applications related to waste-heat recovery, power generation or cooling of electronic devices or small systems.[1-3] So far, a widespread use of this technology has been hampered by the low efficiency of thermoelectric materials which is governed by their dimensionless figure of merit ZT defined as $ZT = \alpha^2 T/\rho\kappa$.[1-3] Achieving high efficiency at a given absolute temperature T requires an unusual combination of high thermopower α, low electrical resistivity ρ and low total thermal conductivity κ. The challenge in designing an ideal thermoelectric material thus lies in scattering efficiently acoustic phonons without causing a concomitant strong reduction in the charge carrier mobility. Materials exhibiting simultaneously high mobility and low lattice thermal conductivity are usually referred to as "phonon glass, electron crystal" (PGEC) in the literature.[4,5]

Materials crystallizing in a complex unit cell provide a possible route to finding novel efficient thermoelectric materials. Their structural complexity gives rise to extremely low lattice thermal conductivity κ_L, the temperature dependence of which often mirrors that of glassy compounds. In addition to Zintl phases, clathrates or cluster compounds,[6-20] complex crystal structures also prevail in homologous compounds.[21,22] Their crystal structure is formed by fundamental building blocks that expand along one or several dimensions by regular increments. The structural complexity can be easily manipulated by varying the number of building blocks which, in turn, offers a tuning parameter of the physical properties. Examples of naturally-occurring homologous series are found in sulfosalt minerals such as the lillianite and pavonite series of general chemical formula $M_{n+1}\mathrm{BiS}_{n+5}$ (M = Ag/Bi or Cu/Bi; $n \geq 2$) and $\mathrm{Pb}_{n-1-2x}\mathrm{Bi}_{2+x}\mathrm{Ag}_x\mathrm{S}_{n+2}$, respectively, with n being either integer or non-integer.[23,24] Recent investigations on the synthetic lillianites $\mathrm{Pb_7Bi_4Se_{13}}$ and $\mathrm{Pb_6Bi_2Se_9}$, both belonging to the series of general formula $Pb_{N-1}Bi_2Se_{N+2}$ with $N = 4.5$ and 7, respectively, have demonstrated their potential as thermoelectric materials.[25,26] These compounds are narrow-band-gap *n*-type semiconductors and remarkably, exhibit very low lattice thermal conductivity (~0.3 W m^{-1} K^{-1} and ~0.9 W m^{-1} K^{-1} at 300 K for $Pb_7Bi_4Se_{13}$ and $Pb_6Bi_2Se_9$, respectively) resulting in a peak *ZT* value of 0.9 at 775 K in $Pb_7Bi_4Se_{13}$.[25]

The minerals called cannizzarite are naturally-occurring Pb-Bi sulfosalt that provide another interesting example of homologous series.[27-33] The crystal structure is composed of pseudo-tetragonal layers (Q) that alternate with a double-octahedron layer (H) of pseudo-hexagonal symmetry. The general formulas of these layers can be written as M_2S_2 and M_4S_6, respectively, where M is Pb/Bi. When m H layers match n Q layers, the structure is referred to as semi-commensurate and then correspond to a variable-fit homologous series written as mH : nQ.[31-33] Various H : Q matches have been predicted and evidenced experimentally in minerals with, among others, the shortest possible type 3H : 5Q that leads to the chemical formula $Pb_5Bi_6S_{14}$.[33]

The selenide counterpart of this last compound belongs to the sub-series $(PbSe)_5(Bi_2Se_3)_{3m}$ (m = 1, 2, 3 and 4) which has recently attracted attention for its interesting physical properties.[34-39] Their crystal structure consists in an alternate stacking of Pb-Se layers separated by m Bi-Se layers interacting via van der Waals gaps. This multilayer heterostructure formed by a topological insulator (Bi_2Se_3) and an ordinary insulator (PbSe) harbors non-trivial topological states for $m = 2$.[40-42] The intercalation of Cu into the van der Waals gap between the two Bi_2Se_3 adjacent layers results in bulk superconductivity at 2.9 K making this system an interesting platform for the search of topological superconductivity.[42] Bulk superconductivity was also observed in the $m = 1$ compound upon inserting Ag atoms that were shown to dope both the Pb-Se and Bi-Se layers by atom probe tomography.[41,43] Investigations of the thermoelectric properties of the $m = 1$ compound evidenced a peak *ZT* of

0.5 at 723 K arising from a combination of *n*-type semiconducting-like electrical properties and very low κ_L values.[37,38]

Although the crystal structure and some physical properties of the m = 1, 2 and 4 compounds have been reported,[34-39] the thermoelectric properties of the stable m = 2 and 3 members (the m = 4 member is metastable) have not been explored in detail so far. In addition, a full determination of the space group and atomic coordinates of the m = 3 compound is still lacking. Here, we report on the synthesis, crystal structure determination and transport properties measurements in a broad range of temperatures (2 – 700 K) of the m = 2 and m = 3 compounds of this series. A combination of single crystal X-ray diffraction, high-resolution transmission electron microscopy (HRTEM), scanning electron microscopy in high-angle annular dark-field mode (STEM – HAADF) was used to provide a precise description of the crystal structure by direct observation of the alternating layers at an atomic scale. In order to determine general trends in the crystal structure and transport properties with varying m, we further characterized the crystal structure and some basic physical parameters of the m = 1 compound. Our results show that both the m = 2 and m = 3 compounds behave as degenerate *n*-type semiconductors. Intriguingly, despite an increase in the structural complexity with increasing m, the lattice thermal conductivity increases concomitantly suggesting that the interfaces between both types of layers play a decisive role in the thermal transport. These two main characteristics yield moderate ZT values that reach ≈ 0.25 and 0.20 at 700 K in the m = 2 and m = 3 compound, respectively.

Experimental Section

Syntheses. All manipulations were carried out in an argon-filled, dry glove box. Polycrystalline samples of the target compositions $Pb_5Bi_{12}Se_{23}$ (m = 2) and $Pb_5Bi_{18}Se_{32}$ (m =

3) were synthesized by a two-step process. In a first step, the two precursors PbSe and Bi_2Se_3 were prepared by direct reaction of stoichiometric quantities of high-purity powders of Pb (99.999%), Bi (99.999%) and Se (99.999%). The mixtures were placed in evacuated quartz tubes sealed under secondary vacuum, heated to 1393 K in a rocking furnace, held at this temperature for 12 h and finally cooled to room temperature over 2 h. In a second step and after verification of phase purity of each precursor by laboratory powder X-ray diffraction, appropriate stoichiometric ratios of PbSe and Bi_2Se_3 were ground into fine powders, pelletized and loaded into evacuated quartz tubes sealed under secondary vacuum. The pellets were annealed for 10 days at 873 K, that is, below the peritectic decomposition temperatures of 973 K and 993 K for the $m = 2$ and $m = 3$ phase, respectively, according to the pseudo-binary phase diagram PbSe – Bi_2Se_3 determined by Zemskov *et al.*[36] After quenching the tubes in room-temperature water, the pellets were reground into fine powders and consolidated in a graphite die by spark plasma sintering at 673 K for 10 min. under a pressure of 80 MPa. The experimental density of the two samples, determined by geometrical dimensions and weight, were above 97% of the theoretical density.

Powder X-ray Diffraction. The crystal structure and phase purity of the precursors and of the final compounds were verified by powder X-ray diffraction (PXRD). These measurements were performed at 300 K using a D8 Bruker Advance diffractometer equipped with a LynxEye detector (Cu $K\alpha_1$ radiation, $\lambda = 1.54056$ Å).

Single Crystal X-ray Diffraction and Structure Determination. Single crystals grown on the surface of the pellets during the annealing treatment could be isolated and employed for crystal structure determinations. The single crystals of needle-like shape (Figure S1 in Supporting Information) were glued on the tip of a quartz fiber and mounted on a goniometer head. Data acquisition was performed at 300 K using a Bruker APEX-II diffractometer equipped with CCD detector using Mo $K\alpha$ radiation ($\lambda = 0.71073$ Å). The structure solution was obtained by direct methods and refined by full-matrix least-squares techniques with the Sir97 and SHELX-2013 softwares, respectively, implemented through the WinGX suite.[44] In agreement with prior studies,[34-37] the intensity data collected for the $m = 2$ compound were best indexed in the monoclinic space group $C2/m$. The crystal structure of the $m = 3$ compound has been successfully solved in the monoclinic space group $P2_1/m$. Possible mixed Pb/Bi occupancies on several Pb crystallographic sites has been suggested in $Pb_5Bi_6Se_{14}$ based on resonant scattering at high energy K-edge experiments.[45] Despite the possibility of similar disorder in the $m = 2$ and 3 compounds, the similar atomic scattering factors of Pb and Bi ($Z = 82$ and 83, respectively) did not allow to consider mixed occupancies in our refinements. We further tried to discriminate the Pb from the Bi atoms by considering bond strength-bond length relationships between Pb^{2+}, Bi^{3+} and Se^{2-} ions using the VALENCE software which is based on the bond valence model.[46,47] The results obtained within this model tend to indicate that the atoms located in the distorted octahedra (atomic positions labeled Pb1 and Pb2 in the following) exhibit a ~ 3+ valence state suggesting that these atoms are in fact mostly Bi atoms. The other atoms in this layer, located in square-based pyramidal polyhedra, are found to exhibit a ~ 2+ valence state consistent with the presence of only Pb atoms. The Pb-Se and Bi-Se distances calculated considering these valence states are in agreement with the refined bond lengths. The two remaining Pb atoms would be then distributed over the 6, 12 and 18 Bi positions in the $m = 1$, 2 and 3 compounds, respectively. The analysis of the Bi-Se interatomic distances does not allow further determining whether Pb preferentially occupies specific positions. It should be kept in mind that this attempt at discriminating both atoms relies on the values used in the valence bond model for the measure of the size of the two ions involved in the bonding, that is, Pb^{2+}-Se^{2-} and Bi^{3+}-Se^{2-}. This tentative assignment should therefore be taken with some caution. Nevertheless, it can be noted that, according to the ionic radii of the Pb^{2+}, Bi^{3+} and Se^{2-} ions, that is, 1.17, 1.33 and

1.84 Å, respectively,[48] the interatomic distances given in Tables 4 and S5 to S7 in the Supporting Information (see below) fairly agree with these above-mentioned hypotheses. In the absence of an unambiguous model for the mixed occupancies, we will consider in the following a structural model where the Pb and Bi atoms occupy distinct layers in agreement with the description of the crystal structure used in the literature.[34-42] The relevant information of data collection and refinements for these two compounds are summarized in Table 1. The atomic coordinates and isotropic displacement parameters for all atoms are given in Table 2 for the m = 3 compound (for comparison, the crystallographic parameters determined for the m = 1 and m = 2 compounds are given in the Supporting Information in Tables S1 to S4). The anisotropic thermal displacement parameters are listed in Table 3. The Pb-Se interatomic distances are gathered in Table 4 for all of the three compounds for comparison purposes while the Bi-Se interatomic distances are provided in Tables S5 to S7 in the Supporting Information.

Scanning Electron Microscopy (SEM). SEM experiments were performed on polished bulk pieces cut from the consolidated ingots using a Quanta FEG 650 (FEI) with energy-dispersive X-ray (EDX) microanalysis. Backscattered electron (BSE) images and elemental X-ray maps were taken to assess phase purity and determine the spatial distribution of Pb, Bi and Se.

Electron Probe Microanalysis (EPMA). Bulk pieces of the consolidated samples were carefully polished using alumina powders. The chemical composition of each specimen was examined by EPMA using a JEOL JXA 8530F instrument equipped with wavelength-dispersive spectrometers. PbTe, elemental Bi and SnSe were used as standards to determine the Pb, Bi and Se concentrations, respectively. The chemical formulae were normalized to 40 and 55 atoms per chemical formula for the m = 2 and m = 3 compounds, respectively.

Transmission Electron Microscopy (TEM). Thin slices were prepared from the single crystals perpendicular to the growth direction (which corresponds to the b axis of the crystal structure) by the dual focused ion beam (FIB) – scanning electron microscope system using the *in-situ* lift-out technique. Scanning TEM (STEM) in high-angle annular dark-field (HAADF) mode, annular bright-field (ABF) and high-resolution TEM (HRTEM) were performed in a JEOL ARM 200F – cold FEG TEM/STEM microscope operating at 200 keV and equipped with a spherical aberration (Cs) probe and image correctors.

Absorption Spectroscopy. Optical measurements were carried out at room temperature on powdered samples using diffuse reflectance spectroscopy on a Thermo Scientific Nicolet 6700 FTIR spectrophotometer equipped with an integrated sphere. Raw reflectance data R were used to estimate the absorption coefficient using the Kubelka-Munk relation $F(R) = (1-R)^2/2R$.[49] The data were then plotted as $(F(R)\hbar\omega)^n$ versus $\hbar\omega$, where $\hbar\omega$ is the incoming photon energy, to estimate the transition onset energies corresponding to the optical band gap E_g. In the absence of electronic band structure calculations, both direct (n = 2) and indirect (n = 1/2) extrapolations of the absorption edge to zero were considered.

Transport properties measurements. Due to the layered crystal structure of the samples, the transport properties were measured on samples cut perpendicular and parallel to the pressing direction in appropriate shape and size with a diamond-wire saw. Electrical resistivity, thermopower and thermal conductivity were measured simultaneously on bar-shaped samples (typical dimensions 2×2×8 mm^3) between 5 and 300 K using the thermal transport option of a physical property measurement system (PPMS, Quantum Design). Good electrical and thermal contacts were ensured by gluing copper bars using conductive silver epoxy. Hall effect measurements were performed on the same samples using a five-probe configuration and the AC transport option of the PPMS. The five copper wires were brazed onto the samples using a low-melting-point braze. The transverse electrical resistivity ρ_{xy} was measured between 5 and 300 K under magnetic fields $\mu_0 H$ ranging between -1 and +1T. Possible magnetoresistive contributions were dismissed by considering the antisymmetric part of ρ_{xy} under magnetic field reversal following the formula $[\rho_{xy}(+\mu_0 H) - \rho_{xy}(-\mu_0 H)]/2$. The Hall electron concentrations n_H and mobilities μ_H were inferred by the single-band formulae $n_H = -1/R_H e$ and $\mu_H = R_H/\rho$ where R_H is the Hall coefficient and e is the elementary charge. The experimental uncertainty associated with the low-temperature measurements of the electrical resistivity, thermopower, thermal conductivity and Hall coefficient are estimated to be 5% for each.

Electrical resistivity and thermopower were measured simultaneously on bar-shaped samples (typical dimensions 1.5×1.5×7 mm^3) between 300 and 700 K under a low-pressure helium atmosphere using a ZEM-3 setup (Ulvac-Riko). The thermal conductivity was determined between 300 and 700 K by combining thermal diffusivity a and specific heat C_p measurements according to the relation $\kappa = \mathrm{a}C_p d$ where d is the experimental density. Thermal diffusivity was measured on graphite-coated disc-shaped (perpendicular direction, 10 mm in diameter and 1 mm in thickness) and prism-shaped (parallel direction, 6×6×1 mm^3) samples by a laser flash technique using a LFA 427 instrument (Netzsch). Specific heat was approximated by the Dulong-Petit law while the temperature dependence of the density has been neglected in the present case. The experimental uncertainty in the measurements of the electrical resistivity, thermopower and thermal conductivity are estimated to be 5%, 5% and 10%, respectively. The combined experimental uncertainty in the *ZT* values is estimated to be 17%.[50]

Results and discussion

Crystal Structure. On the basis of the single-crystal X-ray diffraction data, both compounds crystallize in a monoclinic structure with space group $C2/m$ for m = 2 and $P2_1/m$ for m = 3 (Table 1). The lattice parameters a, b and c and monoclinic angle β obtained for the m = 2 compound are in good agreement with prior diffraction studies.[34-37] The phase purity of the single crystals used for structural characterizations was confirmed by X-ray diffraction performed on ground crystals (not shown). The PXRD results further revealed that single crystals of both the $m = 2$ and $m = 3$ compounds grew simultaneously on the surface of the polycrystalline ingot of the $m = 3$ compound. Surprisingly, a large majority of these single crystals were found to correspond to the $m = 2$ phase. Some crystals of the $m = 3$ compound could nevertheless be isolated.

Figure 1 shows a representation of the crystal structure of the three compounds projected along the *b*-axis. The structure is divided into two alternating structural units made of PbSe-type and Bi_2Se_3-type layers, with the number of Bi-Se layers specified by the integer *m*. The Pb-Se layers correspond to two layers cut perpendicularly to the [100] direction of the *fcc* lattice of PbSe. The Bi-Se layers correspond to five-layer slabs (that is, one quintet) that build the crystal structure of Bi_2Se_3. These two structural units interact via weak Pb/Bi-Se bonds. The misfit between these two types of layers gives rise to strong lattice distortion near the boundaries. Within the Bi-Se layers, Bi atoms show distorted octahedral environments formed by Se atoms (Figure 2). These octahedra share faces to form a two-octahedra thick, slightly modulated ribbon that runs along the *c* axis of the crystal structures. Regardless of *m*, the structure contains five crystallographically independent Pb atoms. Both Pb1 and Pb2 are located at the center of a distorted octahedron. Pb3 and Pb4 atoms occupy an eight-fold coordinated position with tricapped square-based pyramidal geometry while the Pb5 atoms show a seven-fold coordination environment with bicapped square-based pyramidal geometry (see Figure 2). The Pb and Bi atoms in the $m = 2$ and 3 compounds show similar polyhedral environments with varying degree of distortion (Table 4 and Tables S5 to S7 in Supporting Information). In the $m = 2$ compound, the two Bi-Se ribbons are connected by Se-Se bonds with distances varying between 3.436(4) and 3.550(4) Å, reflecting a slight modulation of the ribbons. In the *m* = 3 compound, the Bi_2Se_3 layer intercalated between the two other adjacent Bi_2Se_3 layers (see Figure 1) is formed by two rows of Bi-Se octahedra, which are shifted from each other along the *c* axis. The insertion of this third layer slightly modifies the Se-Se distances observed in the *m* = 2 compound resulting in distances varying between 3.447(2) and 3.546(2) Å.

The results further reveal two important characteristics in the present series of compounds which are nearly insensitive to the value of *m*. First, the Pb atoms exhibit the highest thermal displacement parameters (Table 2 and 3 and S1 to S4 in Supporting Information), with values similar to those typically observed in cage-compounds such as clathrates or skutterudites.[51-53] This first characteristic is not confined to this series and has already been observed in several other Pb-containing sulfide and selenide structures.[25,26,31-33] The second characteristic is tied to the chemical environment of the Pb and Bi atoms. All of the Pb atoms show a distorted environment with short Pb-Se bonds and elongated Pb-Se bonds along the long axis of the polyhedra (Table 4 and Figure 2). Similarly, the Bi atoms exhibit slightly distorted octahedral environment with systematically three short Bi-Se distances of ≈ 2.85 Å and three longer distances of ≈ 3.08 Å (see Tables S5 to S7 in Supporting Information). This strong asymmetric environment is likely the result of the stereoactivity of the Pb^{2+} and Bi^{3+} lone pair electrons.[54,55] Similar distortions attributed to stereoactive lone-pair electrons were also observed in the ternaries $Pb_7Bi_4Se_{13}$ and $Pb_6Bi_2Se_9$ and in the monoclinic compound $K_2Bi_8Se_{13}$ for instance.[25,26,56]

Transmission Electron Microscopy on Single Crystals. For a more detailed structural characterization, high-resolution transmission electron spectroscopy was used to examine the as-grown single crystals of the *m* = 2 and 3 compounds. For comparison purposes, single crystals of the *m* = 1 compound have been also studied. Figure 3 shows the HAADF-STEM images of the *m* = 1, 2 and 3 compounds taken along the [010] zone axis. The corresponding electron diffraction patterns along this axis are also shown. All of the diffraction patterns are consistent with the monoclinic crystal structure of these compounds and can be well indexed with the $P2_1/m$ (m = 1 and 3) and $C2/m$ (m = 2) space groups. Both the lattice parameters and monoclinic distortion angles determined from these patterns are consistent with those refined by single-crystal X-ray diffraction. The high-resolution STEM images agree with the X-ray diffraction data and show the presence of alternating Pb-Se and m Bi-Se structural units. In these images, only the Pb and Bi atoms are visible due to the brightness of the atomic layers which are proportional to Z_n (where Z is the element number of the atom and $1 < n < 2$).[57] The similar Z number of Pb and Bi did not enable us to further distinguish possible mixed occupancies on the Pb and Bi sites. The Se atoms were visualized by collecting annular bright-field (ABF) images (Figure S2 in Supporting Information). No additional modulation of the crystal structure, arising from charge-density waves, additional atomic occupations or insertion between the layers or stacking faults, is observed in the diffraction patterns corresponding to these images. Line profiles (not shown), taken perpendicularly and parallel to the layers, did not provide any clear experimental evidence of the presence of vacancies on the Pb, Bi or Se sites in these single-crystals in agreement with our X-ray diffraction data.

Phase Purity and Chemical Homogeneity of Polycrystalline Specimens. We next turn to the characterizations of the polycrystalline specimens of the m = 2 and 3 compounds. The PXRD patterns (Figure 4) collected on both samples are consistent with the theoretical patterns inferred from the single-crystal X-ray data suggesting the absence of secondary phases within the detection limits of PXRD. Of note, the anisotropic crystal structure of these compounds leads to a strong renormalization of the intensities of the diffraction peaks with the (h00) reflections (equivalent to 00l reflections in the present case) appearing as the most intense peaks in the m = 2 and m = 3 compounds. This preferential orientation did not allow further analyses of these patterns by Rietveld refinements.

SEM analyses performed on both pressed samples (Figure 5) revealed a more complex situation. While the elemental X-ray maps reveal a uniform distribution of Se, some slight but discernable spatial fluctuations in the Pb and Bi concentrations can be observed in these images with Pb-rich (Bi-poor) and Pb-poor (Bi-rich) zones (see Figure 5). This slight inhomogeneous distribution suggests a possible domain of existence at 873 K for each compounds or an exsolution process similar to that observed in tetrahedrites for instance.[58-61] EPMA measurements corroborate this observation and show that the distribution of Pb and Bi corresponds to two phases with close chemical compositions. The average compositions are $Pb_{4.64}Bi_{12.35}Se_{23.20}$ and $Pb_{6.56}Bi_{10.68}Se_{23.20}$ and $Pb_{4.04}Bi_{18.32}Se_{32.52}$ and $Pb_{5.71}Bi_{17.13}Se_{32.52}$ for the $m = 2$ and 3 compounds, respectively. The absence of clear peak splitting or peak broadening in the PXRD patterns suggests that these phases exhibit very similar lattice parameters which is consistent with their close chemical compositions and with the similar ionic radius of Pb^{2+} and Bi^{3+}. Of note, in both compounds, the sum of the Pb and Bi concentrations is found to be close to the expected value (that is, 17 and 23 for the $m = 2$ and 3 compounds, respectively) to within experimental uncertainty.

Optical Measurements. Figure 6 shows the optical absorption spectra collected on the $m = 2$ and $m = 3$ compounds assuming direct transitions (see Figure S3 in Supporting Information for indirect transitions). For comparison, data collected on the $m = 1$ sample are also shown. The spectrum of the $m = 1$ sample shows a very slow increase up to around 0.4 eV where a steep rise is observed which likely corresponds to the optical band gap E_g with an estimated value of 0.43 eV. The featureless and nearly flat increase observed further suggests that this compound is a direct band gap semiconductor. In contrast, the spectra of the $m = 2$ and 3 compounds show a maximum near 0.22 eV followed by a shallow increase up to about 0.4 eV which marks the onset of a faster rise in the absorption. The first absorption edge near 0.15 eV might be associated with interband transitions or with the oscillating electron plasma near the plasma frequency due to the heavily-doped nature of these two compounds (see below). The second increase at higher energies is likely due to optical transitions across the band gap yielding estimated values of 0.38 and 0.40 eV (for direct transitions) and 0.26 and 0.27 eV (for indirect transitions) for the m = 2 and 3 compounds, respectively. While the difference observed between the spectra of the m = 1 and m = 2 compound indicates that the addition of a Bi_2Se_3 layer modifies the electronic band structure of the former, the similar spectra and E_g values on going from m = 2 to m = 3 suggest a weaker influence of the third Bi_2Se_3 layer. In the present case, the slight difference observed between the two E_g values for m = 2 and 3 is likely due to modifications of the electronic band structure by the addition of the third Bi_2Se_3 layer. The influence of the Burstein-Moss effect observed in heavily-doped semiconductors,[62,63] that is, a shift of the optical band gap towards higher energies with increasing the carrier concentration, seems unlikely due to the very similar electron concentrations measured in these two compounds (see below). Should it be direct or indirect, the optical E_g values of these three compounds are in line with those determined for other narrow-band-gap Pb-Bi-Se compounds such as $Pb_7Bi_4Se_{13}$ (0.29 eV) or $Pb_6Bi_2Se_9$ (0.58 eV).[25,26]

Transport Properties. The temperature dependence of the electrical resistivity of the m = 2 and m = 3 compounds is shown in Figure 7a. For the former, ρ increases with increasing temperature below 300 K suggestive of a metallic behavior. The anisotropy between the parallel and perpendicular directions is significant for both compounds with the values measured along the pressing direction being twice higher than those measured perpendicularly. This property indicates that the polycrystalline samples are textured after the SPS process due to the anisotropic crystal structure of these compounds and the strong anisotropy of the electrical properties measured in single crystals.[39] Above 300 K, $\rho(T)$ tends to saturate and varies only weakly upon further warming up to 723 K. The overall complex behavior of the high-temperature part of $\rho(T)$, similar to that observed in the m = 1 compound,[37,38] is no longer visible in the m = 3 sample which features significantly lower ρ values. The nearly linear increase in the whole temperature range indicates a more pronounced metallic character with respect to the m = 1 and 2 compounds.

The general trend observed in the electrical resistivity is confirmed by the temperature dependence of the thermopower (Figure 7b). For both compounds, the α values are isotropic to within experimental uncertainty. As in the m = 1 compound, these two compounds show negative α values suggesting that electrons are the dominant charge carriers. Below 300 K, α increases linearly with temperature up to approximately –30 μV K^{-1} for both compounds. At higher temperatures, the measured values slightly differ with maximum values (in absolute values) of –130 and –100 μV K^{-1} achieved at 723 K for m = 2 and m = 3, respectively.

Both the n-type nature of the transport and the increase in the metallic character on going from m = 1 to m = 3 are consistent with Hall effect measurements carried out below 300 K (Figure 8a). The negative Hall coefficients R_H are in agreement with the sign of the thermopower and nearly temperature independent indicating that both compounds can be viewed as heavily-doped semiconductors. The n-type heavily-doped nature of these two compounds has been attributed to the presence of Bi atoms on the Pb sites which would act as donors assuming Pb^{2+}, Bi^{3+} and Se^{2-} valence states.[45] The increase in the electron concentration on going from m = 1 to m = 2 is thus possibly related to a concomitant increase in the concentration of Bi atoms occupying the Pb positions. The Hall coefficient is not further influenced by the addition of a third Bi-Se layer suggesting that the possible mixed Pb/Bi occupation is similar in the m = 2 and m = 3 compounds.

Within a single-carrier type model, the room-temperature R_H values correspond to electron densities n_H of 2.9×10^{20} and 2.8×10^{20} cm^{-3} for m = 2 and 3, respectively. We note that these two values should be taken with some caution due to the strongly anisotropic crystal structures of these compounds which gives rise to galvanomagnetic properties described by a tensor with up to five independent components.[64] The anisotropy in the R_H values is nevertheless limited in the present case (see Figure 8a) indicating that the above-mentioned values can be considered as reasonable estimates of the actual electron concentrations.

The temperature dependence of the Hall mobility μ_H is shown in Figure 8b. As expected from the layered crystal structure of these compounds, the μ_H values measured in the parallel direction are significantly lower than in the perpendicular direction. The $\mu_H(T)$ curves are similar for both compounds and suggestive of electrons scattered by neutral impurities below ~ 50 K. With increasing temperature, the μ_H values tend to decrease indicating that acoustic phonon scattering becomes dominant above 100 K. What is more surprising, however, is the μ_H values that increase with increasing m in the perpendicular direction. This trend seems to be at odds with the general expectation of a decrease in charge carrier mobility with an increase in the structural complexity of the unit cell. This result suggests that the number of interfaces between the Pb-Se and Bi-Se layers is a critical parameter. As we shall see below, a similar trend is observed for the lattice thermal conductivity.

The total thermal conductivities κ of the m = 2 and m = 3 samples are shown in Figure 9a. The data measured on the m = 1 compound are added for comparison. With no exception, these compounds exhibit glass-like thermal transport marked by the absence of Umklapp maximum at low temperatures and very low κ values in the parallel direction in the whole temperature range. For the m = 2 and m = 3 compounds, the κ values are similar at 300 K (~ 0.7 W m^{-1} K^{-1}) and slightly decrease upon warming to reach ~ 0.6 W m^{-1} K^{-1} at 723 K. The strong anisotropy observed in the ρ values is reversed and of comparable magnitude, with the values measured parallel to the pressing direction roughly twice lower than those measured perpendicular to the pressing direction. The significantly higher values observed in the perpendicular direction for these two compounds reflect their lower electrical resistivity which gives rise to higher electronic contributions to the thermal conductivity.

In order to unveil the trend in the lattice thermal conductivity with m, the electronic contribution has been estimated from the Wiedemann-Franz law $\kappa_e = LT/\rho$ where L is the Lorenz number. The temperature dependence of L was determined using a single parabolic band model as a first approximation. The calculated values vary between 2.45×10^{-8} V^2 K^{-2} at low temperatures for both compounds down to 1.90×10^{-8} and 1.85×10^{-8} V^2 K^{-2} at 723 K in the m = 3 and m = 2 compounds, respectively. The lattice thermal conductivity $\kappa_L = \kappa - \kappa_e$ is very low, approaching 0.5 W m^{-1} K^{-1} at 723 K and only weakly temperature dependent (Figure 9b). The κ_L values have been compared to the minimum thermal conductivity κ_{min} estimated using the transverse v_T and longitudinal v_L sound velocities determined to be 1144 and 1191 m s^{-1} and 2637 and 2382 m s^{-1} for the m = 2 and 3 compounds, respectively.[37,65] At high temperatures, κ_L is close to κ_{min} ≈ 0.30 W m^{-1} K^{-1} indicating only little room for further lowering κ_L.

As seen in the μ_H data, κ_L increases with increasing m in both directions despite an increase in the structural complexity of the unit cell. This variation does not follow the simple and general relationship between κ_L and the volume of the unit cell V observed in several thermoelectric compounds for which κ_L roughly scale as V^{-1}.[66] This unusual trend is another evidence showing that the number of Pb-Se/Bi-Se plays an important role in efficiently scattering acoustic phonons. These data overall imply that further increasing m beyond 3 would most probably result in a further increase in κ_L values and, in the limit of $m \rightarrow \infty$, one would expect κ_L (and probably μ_H) to tend to the values of the binary Bi_2Se_3. The role of the number of interlayer interfaces and the presence of misalignment of lattice planes at these interfaces on κ_L has been also underlined in the $Pb_7Bi_4Se_{13}$ and $Pb_6Bi_2Se_9$ compounds.[25,26] In the latter, the κ_L values show a fourfold increase despite the presence of similar types of alternating layers in both structures.[25,26]

In addition to the number of Pb-Se/Bi-Se interfaces, several other ingredients may contribute to scatter efficiently acoustic phonons resulting in the low κ_L values measured in the $m = 1$ compound. First, the large number of atoms per unit cell results in a large number of optical modes that limit the available phase space for acoustic phonons and give rise to enhanced Umklapp scattering. The large thermal displacement parameters of the Pb atoms are indeed likely associated with low-energy optical modes as observed, for instance, in clathrates or in tetrahedrites.[11-13,70-72] Second, the presence of stereochemically active lone-pair electrons of Pb and Bi likely responsible for the distortion of their octahedral environment might contribute to lowering the thermal transport as recently proposed in the other ternaries $Pb_7Bi_4Se_{13}$ and $Pb_6Bi_2Se_9$ and in several minerals such as tetrahedrites or $CuSbS_2$.[25,26,66,68,70,71] Finally, the possible presence of numerous nanoscale interfaces and stacking faults in polycrystalline specimens, which potentially act as additional phonon scatterers, as observed for instance in $K_2Bi_8Se_{13}$,[56] may also play a significant role in impeding heat transport.

The dimensionless thermoelectric figure of merit *ZT* is shown in Figure 10 as a function of temperature for the $m = 2$ and 3 compounds. Similar peak *ZT* of 0.25 and 0.20 are achieved at 723 K in the $m = 2$ and 3 compounds, respectively. These values are lower than that obtained in the $m = 1$ compound (0.5 at 723 K, Refs. 37 and 38) due to the more pronounced metallic character of these two compounds.

Summary and Conclusion

We reported on a detailed characterization of the crystal structure and transport properties of the $Pb_5Bi_{12}Se_{23}$ and $Pb_5Bi_{18}Se_{32}$ compounds which belongs to the homologous series

$(PbSe)_5(Bi_2Se_3)_{3m}$ with m = 2 and 3. The crystal structure of these compounds, investigated using a combination of single-crystal X-ray diffraction data and high-resolution transmission electron microscopy, consists in alternating Pb-Se and m Bi-Se layers described in the monoclinic space groups $C2/m$ (m = 2) and $P2_1/m$ (m = 3). In contrast to the m = 1 compound which shows a more semiconducting character, the m = 2 and 3 compounds behave as degenerate narrow-band-gap n-type semiconductors possibly due to mixed occupation of Bi and Pb on some sites of the crystal structure. The complex, low-symmetry crystal structure of these compounds results in very low lattice thermal conductivity (0.5 W m^{-1} K^{-1} at 723 K). The comparison of the κ_L and μ_H values in this series indicate that increasing the complexity of the unit cell does not systematically lower the thermal transport and impede charge carrier mobility. Rather, these data underline the essential role played by the number of Pb-Se/Bi-Se interfaces in determining both the electron and phonon transports. These results indicate that their thermoelectric performances might be improved by aliovalent substitutions to drive these compounds closer to a semiconducting state. Furthermore, the possible deviations from the ideal stoichiometry suggested by our chemical analyses require further experimental studies to better understand the complex chemistry of these interesting phases.

Associated Content

Supporting Information

The Supporting Information is available free of charge on the ACS Publications website.

> SEM image of as-grown single-crystals of the $m = 1$ compound, tables S1 to S4 of the crystallographic parameters of the $m = 1$ and 2 compounds, tables S5 to S7 of the Bi-Se interatomic distances for the $m = 1$, 2 and 3 compounds, annular bright-field images collected on single crystals of the $m = 1$, 2 and 3 compounds and optical spectra of the $m = 1$, 2 and 3 compounds assuming indirect transitions. CIF files of the $m = 2$ and $m = 3$ compounds.

Author Information

Corresponding Author

*E-mail for B.L.: bertrand.lenoir@univ-lorraine.fr

ORCID

Christophe Candolfi: 0000-0002-1248-5354

Notes

The authors declare no competing financial interest.

Figure Captions

Figure 1. Crystal structure of $Pb_5Bi_6Se_{14}$ (m = 1), $Pb_5Bi_{12}Se_{23}$ (m = 2) and $Pb_5Bi_{18}Se_{32}$ (m = 3) projected along the *b*-axis showing alternating Pb-Se and Bi-Se structural units. The Pb atoms are in dark grey, the Bi atoms are in purple and the Se atoms are in green. The unit cell for each compound is represented by the blue parallelepiped. Note that, in monoclinic crystal structures, the choice in the definition of the *a* and *c* axis is free so that both axes can be interchanged. In such a case, the *x* and *z* coordinates of all atoms should be interchanged as well.

Figure 2. Coordination polyhedral of Pb and Bi atoms in the m = 3 compound. The chemical environments of these atoms in the m = 1 and 2 compounds are similar.

Figure 3. HAADF-STEM images of the m = 1 (upper left panel), m = 2 (upper middle panel) and m = 3 (right upper panel) single crystals. All these images were taken along the [010] zone axis. A crystal structure overlaid is shown in each panels (Pb atoms in green, Bi atoms in pink and Se atoms in yellow). The lower panels show the corresponding electron diffraction patterns.

Figure 4. Powder X-ray diffraction patterns of the polycrystalline (a) m = 2 and (b) m = 3 compounds synthesized from the PbSe and Bi_2Se_3 precursors. The positions of the Bragg reflections, as calculated from single-crystal X-ray diffraction data, are marked by green vertical ticks. For each compound, the main reflections have been indexed.

Figure 5. SEM images and corresponding X-ray elemental maps of the (a) m = 2 and (b) m = 3 compounds.

Figure 6. Optical absorption spectra for $Pb_5Bi_6Se_{14}$ (m = 1), $Pb_5Bi_{12}Se_{23}$ (m = 2) and $Pb_5Bi_{18}Se_{32}$ (m = 3) plotted as $[F(R) \times E]^2\ vs\ (E = \hbar\omega)$ (that is, for direct transitions). The extrapolation of the solid black lines to zero provides an estimate of the optical band gap E_g.

Figure 7. Temperature dependences of the (a) electrical resistivity and (b) thermopower for $Pb_5Bi_{12}Se_{23}$ (m = 2) and $Pb_5Bi_{18}Se_{32}$ (m = 3). The data of the m = 1 compound (Ref. 38) have been added for comparison. The color-coded symbols are similar in both panels. The solid lines are guides to the eye.

Figure 8. Temperature dependences of the (a) Hall coefficient R_H and (b) Hall mobility μ_H for the m = 1, m = 2 and m = 3 compounds. The color-coded symbols for the m = 2 and 3 compounds are similar in both panels. The data of the m = 1 compound (Ref. 38), shown in green, have been added for comparison. The solid lines are guides to the eye.

Figure 9. (a) Total thermal conductivity κ as a function of temperature for $Pb_5Bi_{12}Se_{23}$ (m = 2) and $Pb_5Bi_{18}Se_{32}$ (m = 3). (b) Temperature dependence of the lattice thermal conductivity κ_L for the m = 2 and m = 3 compounds. For comparison, the data of the m = 1 compound (Ref. 38) have been added. The solid lines are guides to the eye. The horizontal solid black line stands for the minimum thermal conductivity calculated from the experimental sound velocities.

Figure 10. Temperature dependence of the dimensionless thermoelectric figure of merit *ZT* for the *m* =1, *m* = 2 and *m* = 3 compounds. The data of the *m* = 1 compound have been taken from Ref. 38. The solid lines are guides to the eye.

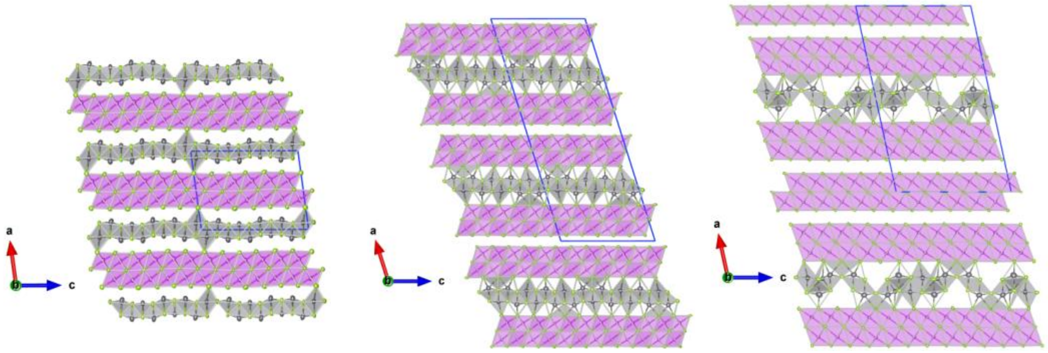

m = 1 m = 2 m = 3

Figure 1

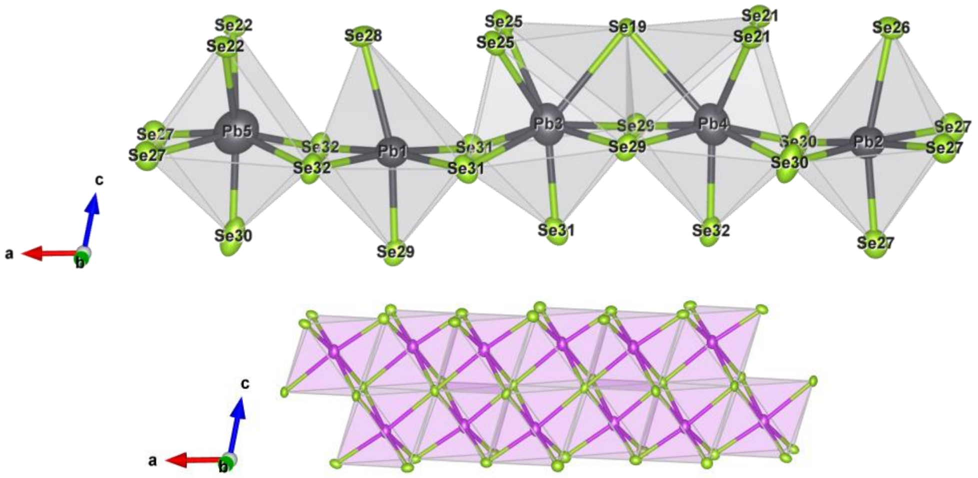

Figure 2

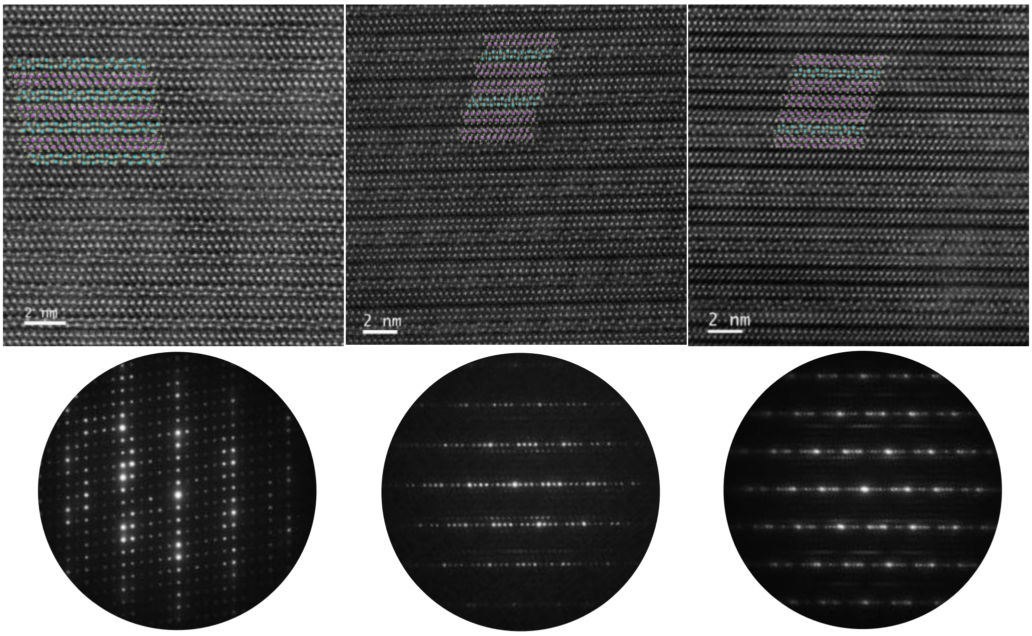

Figure 3

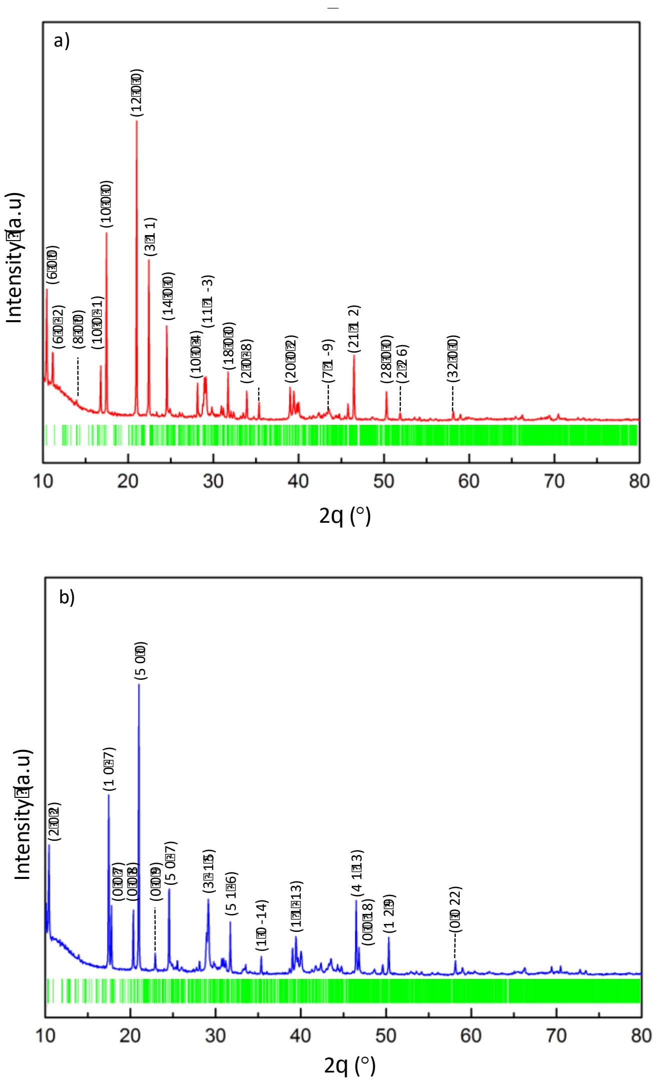

Figure 4

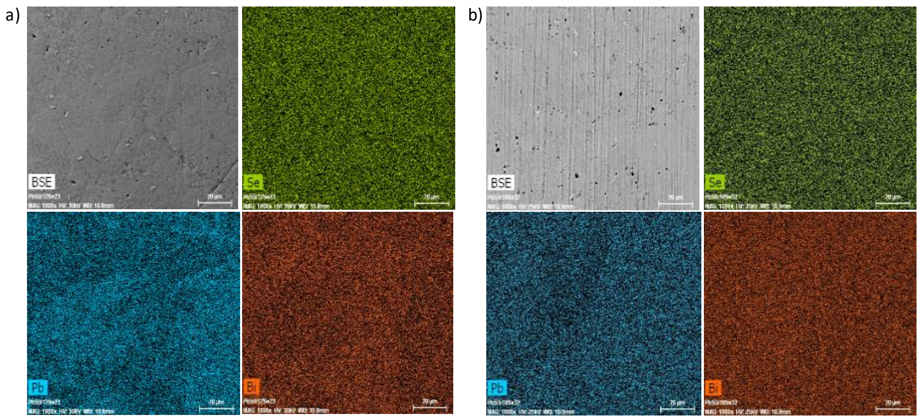

Figure 5

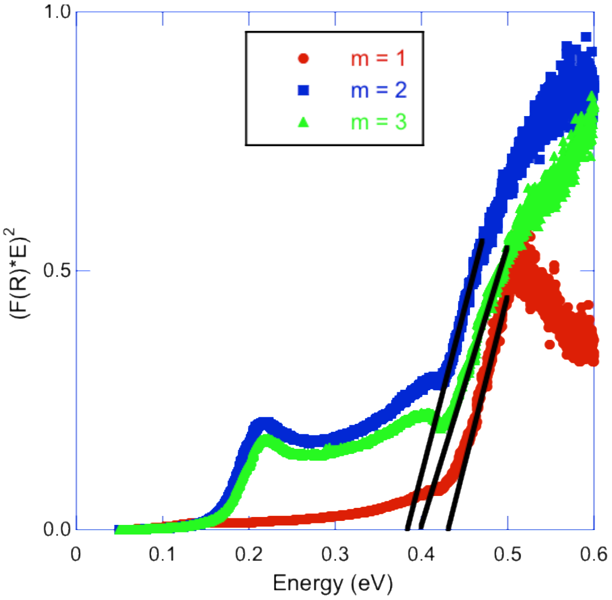

Figure 6

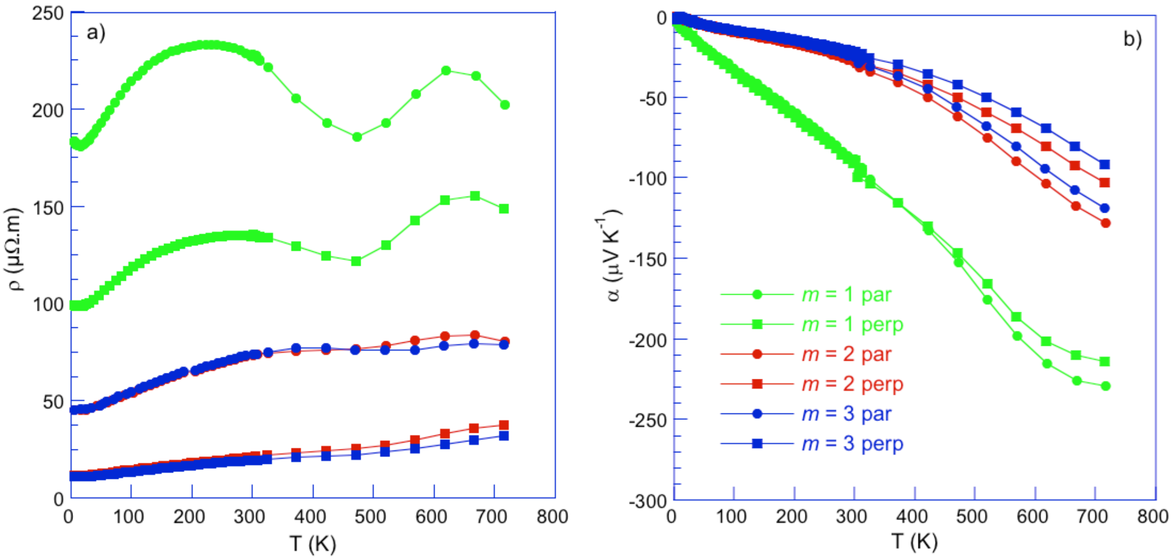

Figure 7

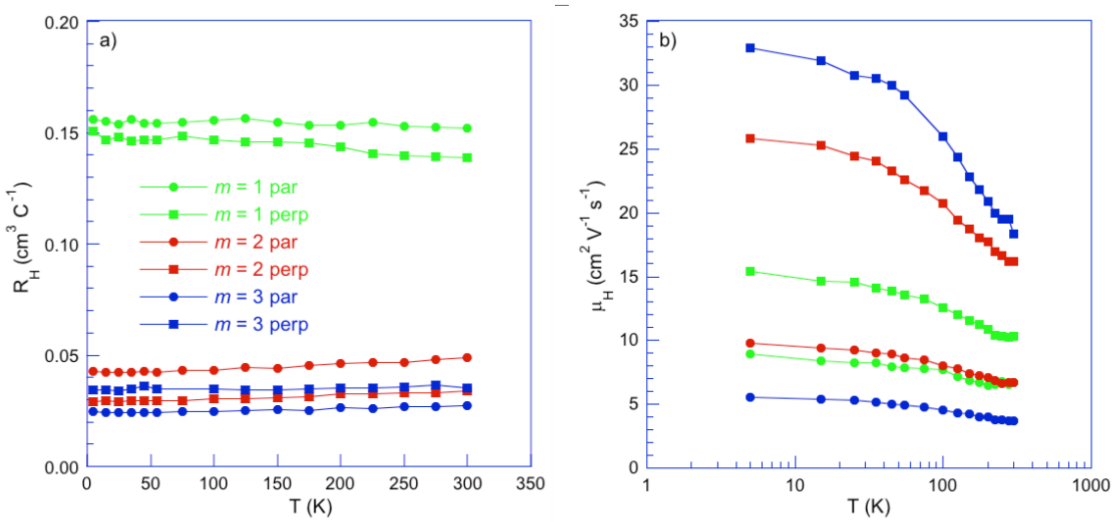

Figure 8

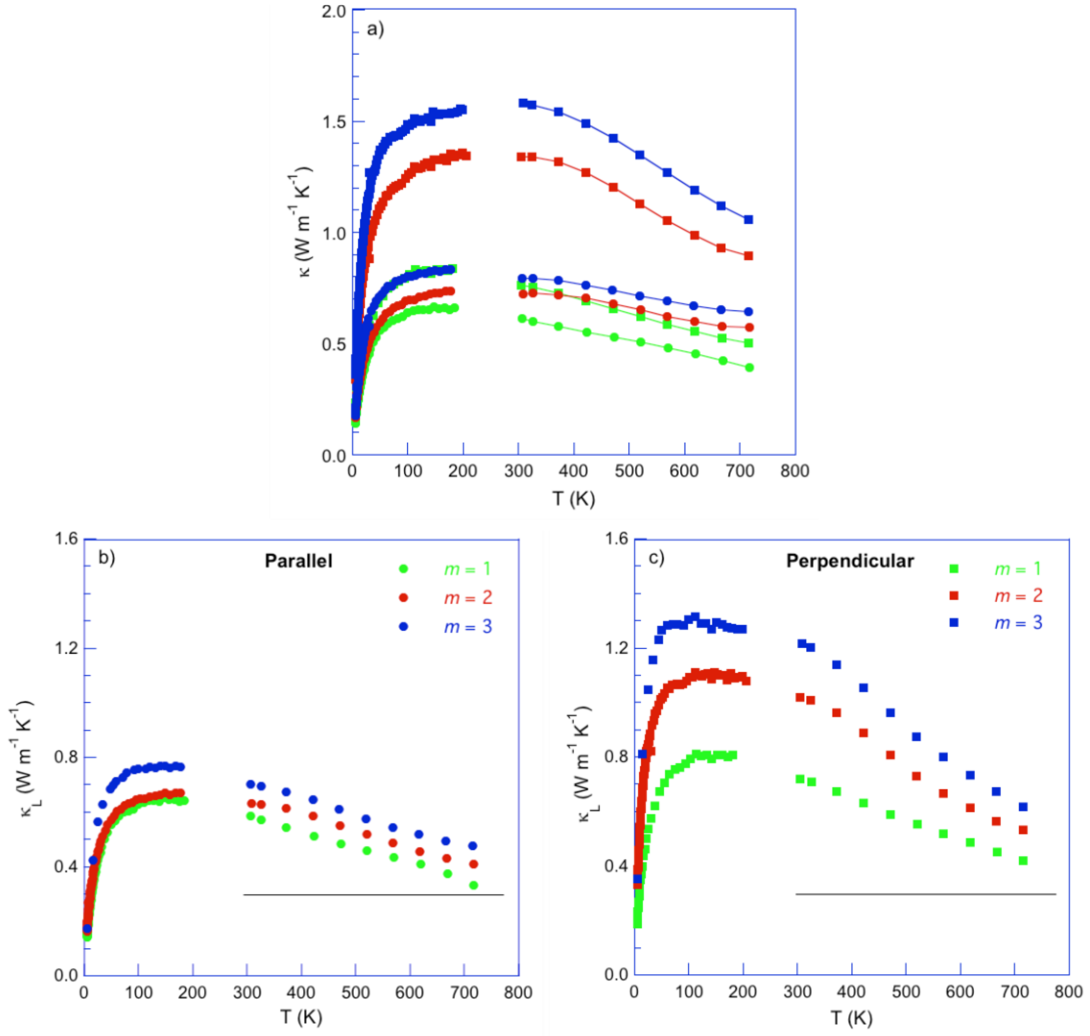

Figure 9

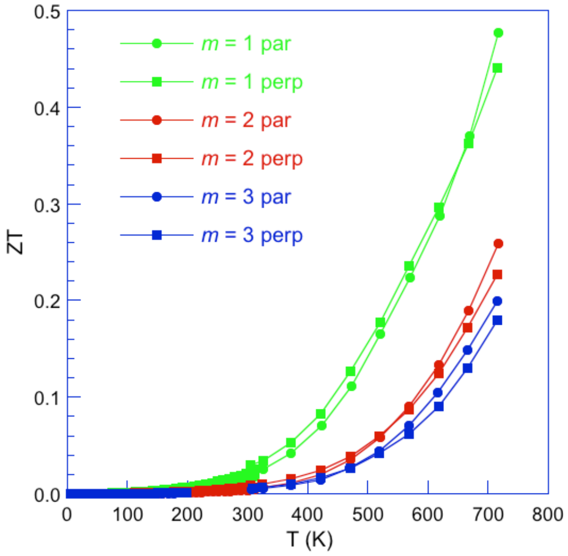
0.5
0.4
0.3
0.2
0.1
0.0
ZT
0
100
200
300
400
500
600
700
800
T (K)
m = 1 par
m = 1 perp
m = 2 par
m = 2 perp
m = 3 par
m = 3 perp

Figure 10

References

(1) Goldsmid, H. J. in *Thermoelectric Refrigeration*; Springer: New York, 1964.

(2) *Thermoelectrics and its Energy Harvesting*, ed. Rowe, D. M., CRC Press, 2012.

(3) Bell, L. Cooling, Heating, Generating Power, and Recovering Waste Heat with Thermoelectric Systems. *Science* **2008**, *321*, 1457−1461.

(4) G. A. Slack in *CRC Handbook of Thermoelectrics* (M. Rowe (Ed.)), CRC Press, Boca Raton, FL (1995).

(5) Chen, Z.-G.; Han, G.; Cheng, L.; Zou, L. Nanostructured thermoelectric materials: Current research and future challenge. *Prog. Nat. Sci.* **2012**, *22*, 535–549.

(6) Brown, S. R.; Kauzlarich, S. M.; Gascoin, F.; Snyder, G. J. $Yb_{14}MnSb_{11}$: New High Efficiency Thermoelectric Material for Power Generation. *Chem. Mater.* **2006**, *18*, 1873−1877.

(7) Bux, S. K.; Zevalkink, A.; Janka, O.; Uhl, D.; Kauzlarich, S. M.; Snyder, G. J.; Fleurial, J.-P. Glass-like Lattice Thermal Conductivity and High Thermoelectric Efficiency in $Yb_9Mn_{4.2}Sb_9$. *J. Mater. Chem. A* **2014**, *2*, 215−220.

(8) Aydemir, U.; Zevalkink, A.; Ormeci, A.; Gibbs, Z. M.; Bux, S.; Snyder, G. J. Thermoelectric Enhancement in $BaGa_2Sb_2$ by Zn Doping. *Chem. Mater.* **2015**, *27*, 1622–1630.

(9) Ortiz, B. R.; Gorai, P.; Stevanovic, V.; Toberer, E. S. Thermoelectric Performance and Defect Chemistry in *n*-type Zintl $KGaSb_4$. *Chem. Mater.* **2017**, *29*, 4523–4534.

(10) Wu, Z.; Li, J.; Li, X.; Zhu, M.; Wu, K.; Tao, X.; Huang, B.-B.; Xia, S. Tuning the Thermoelectric Properties of $Ca_9Zn_{4+x}Sb_9$ by Controlled Doping on the Interstitial Structure. Chem. Mater. 2016, 28, 6917–6924.

(11) Zhang, H.; Borrmann, H.; Oeschler, N.; Candolfi, C.; Schnelle, W.; Schmidt, M.; Burkhardt, U.; Baitinger, M.; Zhao, J.-T.; Grin, Yu. Atomic Interactions in the *p*-Type Clathrate I $Ba_8Au_{5.3}Ge_{40.7}$. *Inorg. Chem.* **2011**, *50*, 1250−1257.

(12) Shi, X.; Yang, J.; Bai, S.; Yang, J.; Wang, H.; Chi, M.; Salvador, J. R.; Zhang, W.; Chen, L.; Wong-Ng, W. On the Design of High-Efficiency Thermoelectric Clathrates through a Systematic Cross-Substitution of Framework Elements. *Adv. Funct. Mater.* **2010**, *20*, 755−763.

(13) Toberer, E. S.; Christensen, M.; Iversen, B. B.; Snyder, G. J. High Temperature Thermoelectric Efficiency in $Ba_8Ga_{16}Ge_{30}$. *Phys. Rev. B* **2008**, *77*, No. 075203.

(14) Kurosaki, K.; Kosuga, A.; Muta, H.; Uno, M.; Yamanaka, S. Ag_9TlTe_5: A High-performance Thermoelectric Bulk Material with Extremely Low Thermal Conductivity. *Appl. Phys. Lett.* **2005**, *87*, No. 061919.

(15) Guo, Q.; Chan, M.; Kuropatwa, B. A.; Kleinke, H. Enhanced Thermoelectric Properties of Variants of Tl_9SbTe_6 and Tl_9BiTe_6. *Chem. Mater.* **2013**, *25*, 4097−4104.

(16) Guo, Q.; Assoud, A.; Kleinke, H. Improved Bulk Materials with Thermoelectric Figure-of- Merit Greater than 1: $Tl_{10-x}Sn_xTe_6$ and $Tl_{10-x}Pb_xTe_6$. *Adv. Energy Mater.* **2014**, *4*, No. 1400348.

(17) Zhou, T.; Lenoir, B.; Colin, M.; Dauscher, A.; Al Orabi, R. A. R.; Gougeon, P.; Potel, M.; Guilmeau, E. Promising Thermoelectric Properties in $Ag_xMo_9Se_{11}$ Compounds ($3.4 \leq x \leq 3.9$). *Appl. Phys. Lett.* **2011**, *98*, No. 162106.

(18) Al Rahal Al Orabi, R.; Fontaine, B.; Gautier, R.; Gougeon, P.; Gall, P.; Bouyrie, Y.; Dauscher, A.; Candolfi, C.; Lenoir, B. Cu Insertion Into the Mo_{12} Cluster Compound $Cs_2Mo_{12}Se_{14}$: Synthesis, Crystal and Electronic Structures, and Physical Properties. *Inorg. Chem.* **2016**, *55*, 6616−6624.

(19) Gougeon, P.; Gall, P.; Al Rahal Al Orabi, R.; Fontaine, B.; Gautier, R.; Potel, M.; Zhou, T.; Lenoir, B.; Colin, M.; Candolfi, C.; Dauscher, A. Synthesis, Crystal and Electronic Structures, and Thermoelectric Properties of the Novel Cluster Compound $Ag_3In_2Mo_{15}Se_{19}$. *Chem. Mater.* **2012**, *24*, 2899−2908.

(20) Al Rahal Al Orabi, R.; Gougeon, P.; Gall, P.; Fontaine, B.; Gautier, R.; Colin, M.; Candolfi, C.; Dauscher, A.; Hejtmanek, J.; Malaman, B.; Lenoir, B. X-ray Characterization, Electronic Band Structure, and Thermoelectric Properties of the Cluster Compound $Ag_2Tl_2Mo_9Se_{11}$. *Inorg. Chem.* **2014**, *53*, 11699–11709.

(21) Mrotzek, A.; Kanatzidis, M. G. “Design” in Solid-State Chemistry Based on Phase Homologies. The Concept of Structural Evolution and the New Megaseries $A_m[M_{1+l}Se_{2+l}]_{2m}[M_{2l+n}Se_{2+3l+n}]$. *Acc. Chem. Res.* **2003**, *36*, 111−119.

(22) Kanatzidis, M. G. Structural evolution and phase homologies for ″design″ and prediction of solid-state compounds. *Acc. Chem. Res.* **2005**, *38*, 359−368.

(23) Makovicky, B.; Mumme, W. C.; Watts, J. A. The Crystals Structure of Synthetic Pavonite, $AgBi_3S_5$, and The Definition of the Pavonite Homologous Series. *Can. Mineral.* **1977**, *15*, 339−348.

(24) Pring, A.; Jercher, M.; Makovicky, E. Disorder and compositional variation in the lillianite homologous series. *Mineral. Mag.* **1999**, *63*, 917−926.

(25) Olvera, A.; Shi, G.; Djieutedjeu, H.; Page, A.; Uher, C.; Kioupakis, E.; Poudeu, P. F. P. $Pb_7Bi_4Se_{13}$: a lillianite homologue with promising thermoelectric properties. *Inorg. Chem.* **2015**, *54*, 746−755.

(26) Casamento, J.; Lopez, J. S.; Moroz, N. A.; Olvera, A.; Djieutedjeu, H.; Page, A.; Uher, C.; Poudeu, P. F. P. Crystal Structure and Thermoelectric Properties of the $_{7,7}L$ Lillianite Homologue $Pb_6Bi_2Se_9$. *Inorg. Chem.* **2017**, *56*, 261−268.

(27) Graham, A. R.; Thompson, R. M.; Berry, L. G. Studies on mineral sulpho-salts: XVII – Cannizzarite. *Am. Mineral.* **1953**, *38*, 536–544.

(28) Matzat, E. Cannizzarite. *Acta Cryst.* **1979**, *B35*, 133–136.

(29) Ferraris, G.; Makovicky, E.; Merlino, S. in *Crystallography of Modular Materials*, Oxford Scholarship, 2008.

(30) Makovicky, E.; Hyde, B. G. Non-commensurate (misfit) layer structures. *Struct. Bonding* **1981**, *46*, 101–170.

(31) Makovicky, E.; Hyde, B. G. in *Incommensurate misfit sandwiched layered compounds*, Ed. A. Meerschaut, Materials Science Forum, vol. 100-101, pp. 1-100, 1992.

(32) Topa, D.; Makovicky, E.; Dittrich, H. The crystal structure of 7K : 12Q cannizzarite from Vulcano, Italy. *Can. Mineral.* **2010**, *48*, 483–495.

(33) Borisov, S. V.; Pervukhina, N. V.; Magarill, S. A.; Kuratieva, N. V.; Bryzgalov, I. A.; Mozgova, N. N.; Chaplygin, I. V. The crystal structure of (Cd, In)-rich cannizzarite from Kudriavy Volcano, Iturup Island, Kuriles, Russia. *Can. Mineral.* **2012**, *50*, 387–395.

(34) Shelimova, L.; Karpinskii, O.; Konstantinov, P.; Avilov, E.; Kretova, M.; Lubman, G.; Nikhezina, I. Y.; Zemskov, V. Composition and properties of compounds in the PbSe-Bi_2Se_3 system. *Inorg. Mater.* **2010**, *46*, 120−126.

(35) Shelimova, L.; Karpinskii, O.; Zemskov, V. X-ray diffraction study of ternary layered compounds in the PbSe-Bi_2Se_3 system. *Inorg. Mater.* **2008**, *44*, 927−931.

(36) Zemskov, V.; Shelimova, L.; Konstantinov, P.; Avilov, E.; Kretova, M.; Nikhezina, I. Y. Thermoelectric materials with low heat conductivity based on PbSe-Bi_2Se_3 compounds. *Inorg Mater: Applied Res.* **2011**, *2*, 405−413.

(37) Ohta, M.; Chung, D. Y.; Kunii, M.; Kanatzidis, M. G. Low lattice thermal conductivity in $Pb_5Bi_6Se_{14}$, $Pb_3Bi_2S_6$, and $PbBi_2S_4$: promising thermoelectric materials in the cannizzarite, lillianite, and galenobismuthite homologous series. *J. Mater. Chem. A* **2014**, *2*, 20048−20058.

(38) Sassi, S.; Candolfi, C.; Ohorodniichuk, V.; Gendarme, C.; Masschelein, P.; Dauscher, A.; Lenoir, B. Thermoelectric Properties of Polycrystalline *n*-Type $Pb_5Bi_6Se_{14}$. *J. Electron. Mater.* **2017**, *46*, 2790–2796.

(39) Segawa, K.; Taskin, A. A.; Ando, Y. $Pb_5Bi_{24}Se_{41}$: A new member of the homologous series forming topological insulator heterostructures. *J. Solid State Chem.* **2015**, *221*, 196–201.

(40) Nakayama, K.; Eto, K.; Tanaka, Y.; Sato, T.; Souma, S.; Takahashi, T.; Segawa, K.; Ando, Y. Manipulation of Topological States and the Bulk Band Gap Using Natural Heterostructures of a Topological Insulator. *Phys. Rev. Lett.* **2012**, *109*, 236804.

(41) Fang, L.; Stoumpos, C. C.; Jia, Y.; Glatz, A.; Chung, D. Y.; Claus, H.; Welp, U.; Kwok, W.-K.; Kanatzidis, M. G. Dirac fermions and superconductivity in the homologous structures $(Ag_xPb_{1-x}Se)_5(Bi_2Se_3)_{3m}$ ($m = 1, 2$). *Phys. Rev. B* **2014**, *90*, 020504(R).

(42) Sasaki, S.; Segawa, K.; Ando, Y. Superconductor derived from a topological insulator heterostructure. *Phys. Rev. B* **2014**, *90*, 220504(R).

(43) Ren, X.; Singh, A. K.; Fang, L.; Kanatzidis, M. G.; Tavazza, F.; Davydov, A. V.; Lauhon, L. J. Atom Probe Tomography Analysis of Ag Doping in 2D Layered Material $(PbSe)_5(Bi_2Se_3)_3$. *Nano Lett.* **2016**, *16*, 6064–6069.

(44) Farrugia, L. J. WinGX and ORTEP for Windows: an update. *J. Appl. Cryst.* **2012**, *45*, 849–854.

(45) Zhang, Y.; Wilkinson, A. P.; Lee, P. L.; Shastri, S. D.; Shu, D.; Chung, D.-Y.; Kanatzidis, M. G. Determining metal ion distributions using resonant scattering at very high-energy K-edges: Bi/Pb in $Pb_5Bi_6Se_{14}$. *J. Appl. Cryst.* **2005**, *38*, 433–441.

(46) VALENCE software, http://www.ccp14.ac.uk/ccp/web-mirrors/valence/.

(47) Brown, I. D. The Chemical Bond in Inorganic Chemistry, The Bond Valence Model; Oxford University Press; Oxford U.K., 2002.

(48) Shannon, R. D. Acta Cryst. **1976**, *A32*, 751–767.

(49) Kubelka, P.; Munk, F. Ein Beitrag Zur Optik Der Farbanstriche. *Z. Tech. Phys.* **1932**, *12*, 593–601.

(50) Alleno, E.; Bérardan, D.; Byl, C.; Candolfi, C.; Daou, R.; Decourt, R.; Guilmeau, E.; Hébert, S.; Hejtmanek, J.; Lenoir, B.; Masschelein, P.; Ohorodniichuk, V.; Pollet, M.; Populoh, S.; Ravot, D.; Rouleau, O.; Soulier, M. A round robin test of the uncertainty on the measurement of the thermoelectric dimensionless figure of merit of $Co_{0.97}Ni_{0.03}Sb_3$. *Rev. Sci. Instrum.* **2015**, *86*, 011301.

(51) Christensen, M.; Johnsen, S.; Iversen, B.B. Thermoelectric clathrates of type I. *Dalton Trans.* **2010**, *39*, 978–992.

(52) Aydemir, U.; Candolfi, C.; Borrmann, H.; Baitinger, M.; Ormeci, A.; Carrillo-Cabrera, W.; Chubilleau, C.; Lenoir, B.; Dauscher, A.; Oeschler, N.; Steglich, F.; Grin, Yu. Crystal structure and transport properties of $Ba_8Ge_{43}\square_3$. *Dalton Trans.* **2010**, *39*, 1078–1088.

(53) Sales, B. C.; Mandrus, D.; Chakoumakos, B. C.; Keppens, V.; Thompson, J. R. Filled Skutterudite Antimonides: Electron Crystals and Phonon Glasses. *Phys. Rev. B* **1997**, *56*, 15081–15089.

(54) Walsh, A.; Payne, D. J.; Egdell, R. G.; Watson, G. W. Stereochemistry of post-transition metal oxides: revision of the classical lone pair model. *Chem. Soc. Rev.* **2011**, *40*, 4455–4463.

(55) Fisher, G. A.; Norman, N. C. The structures of the group 15 element (III) halides and halogenoanions. *Adv. Inorg. Chem.* **1994**, *41*, 233−271.

(56) Pei., Y.; Chang, C.; Wang, Z.; Yin, M.; Wu, M.; Tan, G.; Wu, H.; Chen, Y.; Zheng, L.; Gong, S.; Zhu, T.; Zhao, X.; Huang, L.; He, J.; Kanatizidis, M. G.; Zhao, L.-D. Multiple Converged Conduction Bands in $K_2Bi_8Se_{13}$: A Promising Thermoelectric Material with Extremely Low Thermal Conductivity. *J. Am. Chem. Soc.* **2016**, *138*, 16364–16371.

(57) Pennycook, S. J.; Boatner, L. A. Chemically sensitive structure imaging with a scanning transmission electron microscope. *Nature* **1988**, *336*, 565−567.

(58) Makovicky, E.; Skinner, B. J. Studies of the Sulfosalts of Copper. VI. Low-Temperature Exsolution in Synthetic Tetrahedrite Solid Solution, $Cu_{12+x}Sb_{4+y}S_{13}$. *Can. Mineral.* **1978**, *16*, 611−623.

(59) Tatsuka, K.; Morimoto, N. Tetrahedrite Stability Relations in the Cu-Sb-S System. *Econ. Geol. Bull. Soc. Econ. Geol.* **1977**, *72*, 258−270.

(60) Tatsuka, K.; Morimoto, N. Composition Variation and Polymorphism of Tetrahedrite in the Cu-Sb-System Below 400°C. *Am. Mineral.* **1973**, *58*, 425−434.

(61) Bouyrie, Y.; Candolfi, C.; Dauscher, A.; Malaman, B.; Lenoir, B. Exosultion Process as a Route toward Extremely Low Thermal Conductivity in $Cu_{12}Sb_{4-x}Te_xS_{13}$ Tetrahedrites. *Chem. Mater.* **2015**, *27*, 8354–8361.

(62) Burstein, E. Anomalous Optical Absorption Limit in InSb. *Phys. Rev.* **1954**, *93*, 632–633.

(63) Moss, B. T. The Interpretation of the Properties of Indium Antimonide. *Proc. Phys. Soc. B* **1954**, *67*, 775–782.

(64) Akgöz, Y. C.; Saunders, G. A. Space-time symmetry restrictions on the form of transport tensors. I. Galvanomagnetic effects. *J. Phys. C: Solid State Phys.* **1975**, *8,* 1387–1396.

(65) Cahill, D. G.; Watson, S. K.; Pohl, R. O. Lower limit to the thermal conductivity of disordered crystals. *Phys. Rev. B.* **1992**, *46*, 6131−6140.

(66) Toberer, E. S.; May, A. F.; Snyder, G. J. Zintl Chemistry for Designing High Efficiency Thermoelectric Materials. *Chem. Mater.* **2010**, *22*, 624–634.

(67) Bouyrie, Y.; Candolfi, C.; Pailhès, S.; Koza, M. M.; Malaman, B.; Dauscher, A.; Tobola, J.; Boisron, O.; Saviot, L.; Lenoir, B. From Crystal to Glass-like Thermal Conductivity in Crystalline Minerals. *Phys. Chem. Chem. Phys.* **2015**, *17*, 19751−19758.

(68) Lai, W.; Wang, Y.; Morelli, D. T.; Lu, X. From Bonding Asymmetry to Anharmonic Rattling in $Cu_{12}Sb_4S_{13}$ Tetrahedrites: When Lone-Pair Electrons Are Not So Lonely. *Adv. Funct. Mater.* **2015**, *25*, 3648–3657.

(69) May, A. F.; Delaire, O.; Niedziela, J. L.; Lara-Curzio, E.; Susner, M. A.; Abernathy, D. L.; Kirkham, M.; McGuire, M. A. Structural phase transition and phonon instability in $Cu_{12}Sb_4S_{13}$. *Phys. Rev. B* **2016**, *93*, 064104.

(70) Dong, Y.; Khabibullin, A. R.; Wei, K.; Salvador, J. R.; Nolas, G. S.; Woods, L. M. Bournonite $PbCuSbS_3$: Stereochemically Active Lone-Pair Electrons that Induce Low Thermal Conductivity. *Chem. Phys. Chem.* **2015**, *16*, 3264–3270.

(71) Du, B.; Zhang, R.; Chen, K.; Mahajan, A.; Reece, M. J. The impact of lone-pair electrons on the lattice thermal conductivity of the thermoelectric compound $CuSbS_2$. *J. Mater. Chem. A* **2017**, *5*, 3249–3259.

Tables

Table 1. Selected Crystal data and structure refinements of the $(\mathrm{PbSe})_5(\mathrm{Bi_2Se_3})_{3m}$ phases for $m = 2$ and $m = 3$.

Empirical formula	$\mathrm{Pb_5Bi_{12}Se_{23}}$	$\mathrm{Pb_5Bi_{18}Se_{32}}$
Molar mass (g $\mathrm{mol^{-1}}$)	5360.07	7324.68
Symmetry	Monoclinic	Monoclinic
Space group	$C2/m$	$P2_1/m$
a (Å)	53.168 (4)	35.667 (2)
b (Å)	4.1786 (3)	4.1670 (2)
c (Å)	21.550 (2)	21.530 (1)
β (°)	107.491 (3)	102.275 (2)
V (Å^3)	4566.4 (6)	3126.7 (1)
Z	4	2
ρ_{calc} (g $\mathrm{cm^{-3}}$)	7.79	7.78
2θ range (°)	1.60 – 60.63	1.64 – 50.05
Radiation (Å)	Mo Kα; $\lambda = 0.71073$	Mo Kα; $\lambda = 0.71073$
Absorption coefficient ($\mathrm{mm^{-1}}$)	82.74	82.48
Index range	$-73 \leq h \leq 74$	$-25 \leq h \leq 25$
	$-5 \leq k \leq 5$	$-4 \leq k \leq 4$
	$-30 \leq l \leq 30$	$-42 \leq l \leq 42$
Data/restraints/parameters	7688 / 0 / 242	6356 / 0 / 386
R indices [$F_o > 4\sigma(F_o)$]	R1 = 0.066	R1 = 0.060
	wR2 (all) = 0.2339	wR2 (all) = 0.2151
Goodness-of-fit on F^2	0.963	1.028

Table 2. Atomic coordinates and equivalent isotropic displacement parameters (Å^2) for the $m = 3$ compound. U_{eq} is defined as one-third of the trace of the orthogonalized U_{ij} tensor.

Atom	x	y	z	U_{eq}
Pb1	0.46557(4)	1/4	0.33733(6)	0.0194(3)
Pb2	0.53820(4)	3/4	0.06768(7)	0.0217(3)
Pb3	0.55452(4)	3/4	0.47393(7)	0.0259(3)
Pb4	0.55342(4)	3/4	0.26733(7)	0.0281(3)
Pb5	0.55116(5)	3/4	0.86364(8)	0.0367(4)
Bi1	0.94543(4)	1/4	0.67609(6)	0.0102(3)
Bi2	0.94450(4)	3/4	0.17447(6)	0.0103(3)
Bi3	0.78526(4)	3/4	0.45390(6)	0.0100(2)
Bi4	0.67284(4)	3/4	0.96965(6)	0.0128(3)
Bi5	0.78313(4)	3/4	0.11822(6)	0.0110(3)
Bi6	0.78353(4)	1/4	0.62002(6)	0.0106(3)
Bi7	0.94521(4)	3/4	0.50900(6)	0.0094(4)
Bi8	0.94472(4)	1/4	0.34155(6)	0.0098(4)
Bi9	0.67444(4)	1/4	0.47056(6)	0.0109(3)
Bi10	0.94524(4)	3/4	0.84246(6)	0.0087(4)
Bi11	0.67253(4)	3/4	0.63456(6)	0.0120(3)
Bi12	0.78131(4)	1/4	-0.95090(6)	0.0110(3)
Bi13	0.94467(4)	1/4	0.00825(6)	0.0099(3)
Bi14	0.67235(4)	1/4	0.13808(6)	0.0125(3)
Bi15	0.78437(4)	1/4	0.28614(6)	0.0098(3)
Bi16	0.78171(4)	3/4	0.78484(6)	0.0112(3)
Bi17	0.66988(4)	1/4	0.80120(6)	0.0125(3)
Bi18	0.67671(4)	3/4	0.30510(6)	0.0107(3)
Se1	0.82758(10)	1/4	0.18803(16)	0.0107(7)
Se2	0.82748(10)	3/4	0.69205(16)	0.0108(7)

Se3	0.82566(10)	1/4	0.85612(16)	0.0106(6)
Se4	0.82884(10)	3/4	0.35695(16)	0.0092(7)
Se5	0.90078(10)	3/4	0.60524(16)	0.0088(7)
Se6	0.89972(10)	1/4	0.10295(16)	0.0099(6)
Se7	0.82596(10)	3/4	0.02101(16)	0.0101(6)
Se8	0.90051(10)	1/4	0.43814(16)	0.0080(8)
Se9	0.82900(10)	1/4	0.52610(16)	0.0096(8)
Se10	0.89993(10)	3/4	0.27032(16)	0.0091(6)
Se11	0.90001(10)	3/4	0.93674(16)	0.0113(6)
Se12	0.72514(10)	1/4	0.04404(15)	0.0089(6)
Se13	0.90056(10)	1/4	0.77122(16)	0.0103(7)
Se14	0.00026(10)	1/4	0.58365(13)	0.0087(6)
Se15	0.72431(9)	3/4	0.87566(15)	0.0099(7)
Se16	0.72745(9)	3/4	0.21092(12)	0.0090(6)
Se17	0.72504(9)	1/4	0.70877(15)	0.0097(6)
Se18	0.00064(8)	3/4	0.75073(13)	0.0085(7)
Se19	0.62962(9)	3/4	0.39928(15)	0.0079(7)
Se20	0.72785(9)	3/4	0.54454(15)	0.0075(6)
Se21	0.62926(9)	1/4	0.23754(16)	0.0130(6)
Se22	0.62586(9)	1/4	0.89716(16)	0.0113(6)
Se23	0.72978(9)	1/4	0.37853(15)	0.0083(7)
Se24	0.99969(8)	3/4	0.08286(13)	0.0069(7)
Se25	0.62669(9)	1/4	0.55883(16)	0.0115(6)
Se26	0.62726(9)	3/4	0.06759(16)	0.0128(6)
Se27	0.54111(9)	1/4	0.96761(15)	0.0142(6)
Se28	0.62495(10)	3/4	0.72916(14)	0.0143(7)
Se29	0.54429(9)	1/4	0.36649(14)	0.0104(6)
Se30	0.53043(10)	1/4	0.15859(16)	0.0185(7)
Se31	0.47160(9)	3/4	0.43678(15)	0.0122(6)
Se32	0.46990(9)	3/4	0.24254(15)	0.0130(6)

Table 3. Anisotropic thermal displacement parameters (Å^2) for the m = 3 compound at 300 K. By symmetry, U_{23} and U_{12} are both equal to zero for all atoms.

Atom	U_{11}	U_{22}	U_{33}	U_{13}
Pb1	0.0180(5)	0.0191(7)	0.0207(6)	0.0034(1)
Pb2	0.0200(6)	0.0213(7)	0.0233(6)	0.0035(2)
Pb3	0.0349(7)	0.0195(8)	0.0241(6)	0.0080(4)
Pb4	0.0341(7)	0.0254(8)	0.0266(6)	0.0105(4)
Pb5	0.0387(8)	0.0322(9)	0.0370(8)	0.0027(7)
Bi1	0.0126(5)	0.0103(9)	0.0082(5)	0.0031(5)
Bi2	0.0130(5)	0.0105(7)	0.0078(5)	0.0033(1)
Bi3	0.0117(5)	0.0110(6)	0.0074(5)	0.0022(1)
Bi4	0.0152(5)	0.0135(6)	0.0103(5)	0.0036(2)
Bi5	0.0130(5)	0.0131(6)	0.0074(5)	0.0030(1)
Bi6	0.0127(5)	0.0120(7)	0.0071(5)	0.0023(3)
Bi7	0.0127(5)	0.0082(9)	0.0075(5)	0.0026(5)
Bi8	0.0117(5)	0.0105(9)	0.0074(5)	0.0027(1)
Bi9	0.0126(5)	0.0122(6)	0.0082(5)	0.0031(7)
Bi10	0.0133(5)	0.0053(1)	0.0081(5)	0.0029(8)
Bi11	0.0158(5)	0.0113(7)	0.0090(5)	0.0027(6)
Bi12	0.0136(5)	0.0122(6)	0.0078(5)	0.0033(8)
Bi13	0.0133(5)	0.0093(9)	0.0079(5)	0.0037(9)
Bi14	0.0168(5)	0.0114(8)	0.0097(5)	0.0034(2)
Bi15	0.0118(5)	0.0107(7)	0.0074(5)	0.0031(2)
Bi16	0.0138(5)	0.0123(6)	0.0077(5)	0.0027(5)
Bi17	0.0167(5)	0.0119(7)	0.0094(5)	0.0038(3)
Bi18	0.0131(5)	0.0118(7)	0.0075(5)	0.0026(6)
Se1	0.0059(2)	0.0164(1)	0.0094(3)	0.0010(4)
Se2	0.0093(3)	0.0137(9)	0.0090(3)	0.0011(6)
Se3	0.0067(3)	0.0159(7)	0.0088(3)	0.0006(1)
Se4	0.0061(2)	0.0116(1)	0.0098(3)	0.0015(9)
Se5	0.0084(3)	0.0095(1)	0.0085(3)	0.0019(2)

Se6	0.0062(2)	0.0146(7)	0.0088(3)	0.0014(8)
Se7	0.0090(3)	0.0093(8)	0.0121(3)	0.0024(5)
Se8	0.0059(2)	0.0091(2)	0.0098(4)	0.0031(5)
Se9	0.0055(2)	0.0128(3)	0.0095(3)	-0.0011(1)
Se10	0.0055(2)	0.0117(8)	0.0099(3)	0.0008(1)
Se11	0.0091(3)	0.0151(8)	0.0099(4)	0.0023(8)
Se12	0.0089(3)	0.0112(8)	0.0069(3)	0.0024(9)
Se13	0.0065(3)	0.0148(9)	0.0096(3)	0.0016(1)
Se14	0.0076(3)	0.0142(8)	0.0042(2)	0.0011(1)
Se15	0.0117(3)	0.0116(1)	0.0065(3)	0.0017(5)
Se16	0.0087(3)	0.0121(8)	0.0070(3)	0.0029(6)
Se17	0.0105(3)	0.0112(8)	0.0072(3)	0.0014(2)
Se18	0.0086(4)	0.0119(1)	0.0056(3)	0.0024(9)
Se19	0.0064(2)	0.0116(9)	0.0059(2)	0.0015(3)
Se20	0.0076(2)	0.0080(8)	0.0066(3)	0.0003(1)
Se21	0.0096(3)	0.0179(8)	0.0113(3)	0.0020(3)
Se22	0.0091(3)	0.0129(7)	0.0129(3)	0.0042(7)
Se23	0.0085(3)	0.0101(8)	0.0066(3)	0.0024(2)
Se24	0.0077(3)	0.0077(8)	0.0047(2)	-0.0001(4)
Se25	0.0117(3)	0.0133(6)	0.0109(3)	0.0049(2)
Se26	0.0098(3)	0.0145(7)	0.0147(4)	0.0039(5)
Se27	0.0163(4)	0.0139(7)	0.0130(4)	0.0043(7)
Se28	0.0083(3)	0.0182(8)	0.0154(4)	0.0002(7)
Se29	0.0139(4)	0.0069(7)	0.0097(4)	0.0009(5)
Se30	0.0296(6)	0.0136(9)	0.0099(4)	-0.0007(8)
Se31	0.0156(3)	0.0096(7)	0.0130(3)	0.0066(8)
Se32	0.0179(4)	0.0120(7)	0.0084(3)	0.0010(2)

Table 4. Comparison of the Interatomic Distances ($d < 4$ Å) for the Pb Atoms in the Series $(PbSe)_5(Bi_2Se_3)_{3m}$ ($m = 1$, 2 and 3) at 300 K. The indices of the Pb*i* atoms correspond to the indices used in the atomic coordinate tables. ([a] The indices of the Se*i* atoms are referenced according to Figure 2). The mean value of the interatomic distances is also given for the octahedral and square-based pyramidal environments of the five atoms to underline that both Pb1 and Pb2 show distances that are in agreement with a ~ 3+ valence state according to the valence bond model (Ref. 47) suggesting that both sites might be mostly occupied by Bi atoms.

$Pb_5Bi_6Se_{14}$		$Pb_5Bi_{12}Se_{23}$		$Pb_5Bi_{18}Se_{32}$ [a]	
Bond types	Distances	Bond types	Distances	Bond types	Distances
Pb1– Se	2.760(5)	Pb1 – Se	2.743(4)	Pb1 – Se29	2.742(3)
Pb1– Se (×2)	2.936(4)	Pb1 – Se (×2)	2.957(3)	Pb1 – Se32 (×2)	2.943(2)
Pb1– Se (×2)	2.974(4)	Pb1 – Se (×2)	2.959(2)	Pb1 – Se31 (×2)	2.962(2)
Pb1– Se	3.215(6)	Pb1 – Se	3.242(4)	Pb1 – Se28	3.241(3)
Mean value	2.966		2.969		2.960
Pb2 – Se	2.806(6)	Pb2 – Se	2.776(4)	Pb2 – Se27	2.768(3)
Pb2 – Se (×2)	2.921(4)	Pb2 – Se (×2)	2.921(3)	Pb2 – Se30 (×2)	2.911(2)
Pb2 – Se (×2)	3.008(4)	Pb2 – Se (×2)	3.014(3)	Pb2 – Se27 (×2)	3.014(2)
Pb2 – Se	3.116(5)	Pb2 – Se	3.171(3)	Pb2 – Se26	3.177(3)
Mean value	2.963		2.969		2.960
Pb3 – Se	2.935(6)	Pb3 – Se	2.905(4)	Pb3 – Se31	2.895(4)
Pb3 – Se (×2)	3.085(4)	Pb3 – Se (×2)	3.084(2)	Pb3 – Se29 (×2)	3.076(2)
Pb3 – Se (×2)	3.133(4)	Pb3 – Se (×2)	3.116(3)	Pb3 – Se31 (×2)	3.109(3)
Pb3 – Se	3.417(4)	Pb3 – Se	3.407(3)	Pb3 – Se19	3.404(3)
Pb3 – Se (×2)	3.445(3)	Pb3 – Se (×2)	3.497(3)	Pb3 – Se25 (×2)	3.508(3)
Mean value	3.074		3.061		3.050
Pb4 – Se	2.908(6)	Pb4 – Se	2.911(4)	Pb4 – Se32	2.912(3)
Pb4 – Se (×2)	3.054(4)	Pb4 – Se (×2)	3.052(3)	Pb4 – Se29 (×2)	3.050(2)

Pb4 – Se (×2)	3.135(4)	Pb4 – Se (×2)	3.115(2)	Pb4 – Se30 (×2)	3.111(2)
Pb4 – Se	3.508(4)	Pb4 – Se	3.498(3)	Pb4 – Se19	3.489(3)
Pb4 – Se (×2)	3.555(4)	Pb4 – Se (×2)	3.587(2)	Pb4 – Se21 (×2)	3.578(3)
Mean value	3.057		3.049		3.050
Pb5 – Se	2.910(5)	Pb5 – Se	2.869(4)	Pb5 – Se30	2.847(3)
Pb5 – Se (×2)	3.059(4)	Pb5 – Se (×2)	3.063(2)	Pb5 – Se32 (×2)	3.066(2)
Pb5 – Se (×2)	3.148(4)	Pb5 – Se (×2)	3.147(3)	Pb5 – Se27 (×2)	3.133(2)
Pb5 – Se (×2)	3.337(5)	Pb5 – Se (×2)	3.343(3)	Pb5 – Se22 (×2)	3.338(3)
Mean value	3.065		3.057		3.049

For Table of Contents Only

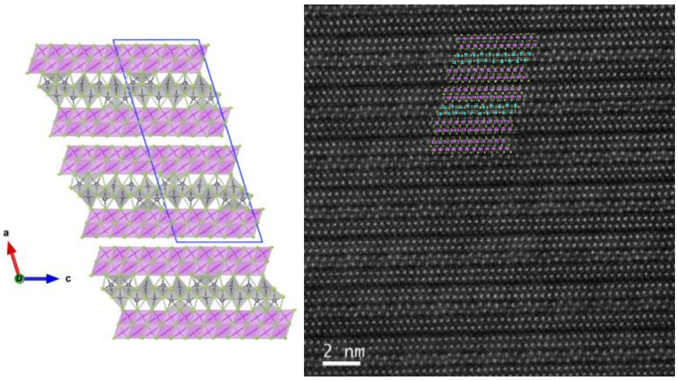

The crystal structure of the homologous compounds $(PbSe)_5(Bi_2Se_3)_{3m}$ for $m = 2$ and 3 has been examined by high-resolution transmission microscope and single-crystal X-ray diffraction. Their transport properties, investigated in a broad temperature range, revealed that both compounds behave as *n*-type degenerate semiconductors and show moderate thermoelectric performances at high temperatures due to too high electron concentrations.